Spatially modulated magnetic structure of EuS due to the tetragonal domain structure of SrTiO_{3}

Aaron J. Rosenberg, Ferhat Katmis, John R. Kirtley, Nuh Gedik, Jagadeesh S. Moodera, and Kathryn A. Moler

Phys. Rev. Materials **1**, 074406 — Published 15 December 2017

DOI: 10.1103/PhysRevMaterials.1.074406

Spatially modulated magnetic structure of EuS due to the tetragonal domain structure of $SrTiO_3$

Aaron J. Rosenberg,[1] Ferhat Katmis,[2,3] John R. Kirtley,[1] Nuh Gedik,[3] Jagadeesh S. Moodera,[2,3] and Kathryn A. Moler[1,4,5]

[1]*Department of Applied Physics, Stanford University, Stanford, CA 94305, USA*

[2]*Fracsis Bitter Magnetic Lab, Massachusetts Institute of Technology, 77 Massachusetts Avenue, Cambridge, Massachusetts 02139, USA*

[3]*Department of Physics, Massachusetts Institute of Technology, 77 Massachusetts Avenue, Cambridge, Massachusetts 02139, USA*

[4]*Department of Physics, Stanford University, Stanford, California 94305, USA*

[5]*Stanford Institute for Materials and Energy Sciences, SLAC National Accelerator Laboratory, 2575 Sand Hill Road, Menlo Park, California 94025, USA*

The combination of ferromagnets with topological superconductors or insulators allows for new phases of matter that support excitations such as chiral edge modes and Majorana fermions. EuS, a wide-band-gap ferromagnetic insulator with a Curie temperature around 16 K, and $SrTiO_3$ (STO), an important substrate for engineering heterostructures, may support these phases. We present scanning superconducting quantum interference device (SQUID) measurements of EuS grown epitaxially on STO that reveal micron-scale variations in ferromagnetism and paramagnetism. These variations are oriented along the STO crystal axes and only change their configuration upon thermal cycling above the STO cubic-to-tetragonal structural transition temperature at 105 K, indicating that the observed magnetic features are due to coupling between EuS and the STO tetragonal structure. We speculate that the STO tetragonal distortions may strain the EuS, altering the magnetic anisotropy on a micron-scale. This result demonstrates that local variation in the induced magnetic order from EuS grown on STO needs to be considered when engineering new phases of matter that require spatially homogeneous exchange.

EuS is a well-studied wide-band-gap ferromagnetic insulator with a NaCl-type structure (lattice constant of 5.94 Å) and a bulk Curie temperature of 16.8 K[1–3]. It has historically been used as an efficient spin filter to spin-polarize charge currents.[4–9]. Because EuS is considered a simple Heisenberg ferromagnet (a ferromagnet that can orient an any 3D direction[10]), it has long been considered a model system to test theories of magnetism[11–14]. EuS has been of recent interest because it may induce magnetic order in topologically non-trivial systems[15,16]. For example, 3D topologically insulating Bi_2Se_3[17–21] has been combined with EuS to induce high-temperature ferromagnetism in the Bi_2Se_3[22]. Additional potential applications include the creation of topological superconductivity to produce zero-energy Majorana fermion modes[23,24], the topological magneto-electric effect[25,26], a magnetic monopole[27], and the quantum anomalous Hall effect[28,29]. In the latter example, one could grow a heterostructure of EuS/topological insulator/EuS with the intention of breaking time reversal symmetry on the top and bottom surface states in order to observe chiral edge modes[25].

$SrTiO_3$ (STO) is a common substrate for growing new heterostructures such as high-temperature superconductors[30–32], ferroelectrics[33,34], and electronic systems with high spin-orbit coupling[35]. STO is a per-

ovskite band insulator with a cubic unit cell. Excitingly, it becomes an unconventional superconductor when doped[36,37], and the interface between STO and another perovskite band insulator, $LaAlO_3$, is both conducting[38,39] and superconducting[40]. At 105 K, STO undergoes a cubic-to-tetragonal structural phase transition because of small rotations of the Ti-O octahedra that causes the unit cell to elongate along one of the crystallographic axes[41]. Without external strain, the STO unit cell can elongate along any of the original cubic axes forming structural domains separated by twin planes. In terms of the original cubic directions, the twin planes are along $(110)_p$, $(101)_p$, and $(011)_p$. Recent studies have shown that the low-temperature twin structure affects both the interfacial conductivity in $LaAlO_3/SrTiO_3$ heterostructures[42,43] and the superconducting transition temperature in STO[44].

We measured the magnetic spatial landscape in four EuS/STO-based heterostructures using a scanning superconducting quantum interference device (SQUID) susceptometer in a ^{4}He cryostat. Unless otherwise indicated, the data in this manuscript were taken on a thin film (5 nm) of $(001)_p$-oriented EuS grown on a $(001)_p$-oriented STO substrate, but we observed similar effects in samples with $(110)_p$- and $(111)_p$-oriented STO substrates, and samples with 3 nm thick EuS[45].

The SQUID sensor measures the total flux through the pickup loop, which is integrated with the body of the SQUID through well-shielded superconducting coaxial leads. The pickup loop size and height above the surface determine the spatial resolution. The pickup loop has an inner radius of 1 μm and an outer radius of 1.5 μm, resulting in an effective radius of 1.24μm[46]. The pickup loop is centered in a single-turn field coil with a 2.5 μm inner radius that can be used to apply a local magnetic field to the sample. Using this sensor, we simultaneously probed the static ferromagnetism (magnetometry) as well as the susceptibility (susceptometry) of the sample[47]. Magnetometry imaging was carried out by measuring the magnetic flux through the SQUID pickup loop, which is the z-component of the magnetic field produced by the sample convolved with the pickup loop's point-spread function. Susceptometry involved applying a small alternating current (ac) current to the field coil and recording the flux through the pickup loop using standard lock-in techniques[48]. To image, we fixed the SQUID sensor above the sample and rastered the sample in the x-y plane using an attocube piezoelectric stack. We thermally coupled the SQUID sensor directly to the liquid helium bath, and we thermally isolated the sample and heater, allowing us to study the magnetic behavior of the sample even at temperatures higher than the superconducting transition temperature of the SQUID (T_C = 9 K).

Epitaxial EuS growth and STO substrate preparation were performed in a custom-built molecular beam epitaxy system under base pressure of 2×10^{-10} Torr. The system is equipped with ultra high-purity source materials for *in situ* growth and protection of the films, as well as units to monitor the thickness of the layer during growth. The interface formation and structural evolution of the grown layer were displayed via an *in situ* reflection high-energy electron diffraction (RHEED) apparatus. The STO epi-ready substrate was prepared in situ after several heat treatments to form an atomically flat surface, which was ensured via RHEED (Fig. 1(a) inset).

Due to the high reactivity of europium atoms and dissociation problems with sulfur, the EuS was evaporated congruently from a single electron-beam source. To avoid kinetic surface roughening, a $\simeq$ 1 - 3 Å min^{-1} growth rate was used to produce a quasi-smooth surface at 523 - 563 K. Layers were grown at 523 K and annealed after growth at 563 K until the layer quality was optimized, as determined via analysis of the RHEED pattern (Fig. 1(a), (b)). Even high-temperature growth does not provide sufficient surface mobility to the EuS molecules; therefore, surface roughening occurs above a critical thickness of 3-4 nm[15,22]. While annealing the film after the growth (Fig. 1(c), (d)), quasi-2D layer streaks transformed into mostly 2D modes, indicating surface smoothing after annealing, which

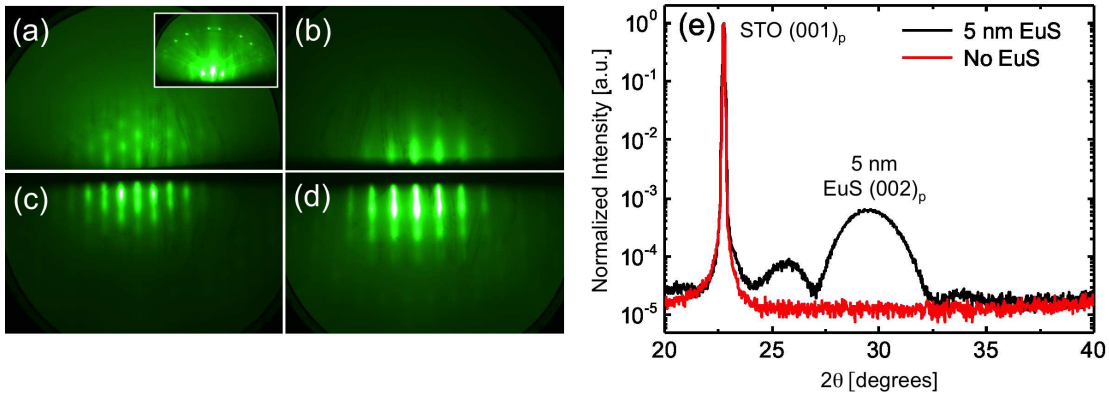

FIG. 1: Captured RHEED patterns of EuS after growth and annealing are shown in (a)-(d). RHEED snap-shot taken with 15 keV electron beam along the $[110]_p$-azimuth (a) and $[001]_p$-azimuth (b) after growth and annealing, respectively, (c) and (d). (e) X-ray diffraction of the EuS/STO heterostructure (black line) and STO substrate without EuS layer (red line). Besides the characteristic intense substrate reflection at the low angle side, another reflection is visible around $\simeq 29.5°$, which belongs to the $(002)_p$ reflection of EuS. The representative data also shows pronounced Laue oscillations (oscillations in the vicinity of the EuS Bragg peak), which indicate the coherency of the top and the bottom surface parallelism of the epitaxial EuS layer.

helped to form a smooth EuS layer. As a final step, films were covered *in situ* with ≃5 nm amorphous Al_2O_3 at room temperature as a protection layer in the same deposition chamber.

In order to obtain detailed information on the crystal structure, the films were investigated by X-ray based diffraction in addition to RHEED. A well-collimated nearly background-free beam is impinged on the sample surface and the scattered X-ray intensity is collected by a two-dimensional CCD camera. The incoming beam is diffracted by a Ge (220) 4-bounce crystal monochromator to get Cu-$K_{\alpha 1}$ radiation (wavelength λ=1.54056 Å) over a wide range of diffraction angles. The X-ray diffraction pattern at room temperature shows two major Bragg peaks in Fig. 1(e). The more intense peak corresponds to the substrate, while the less intense one at around $\simeq 29.5°$ corresponds to Bragg reflection from the 5 nm EuS ($[002]_p$) layer indicating that the substrate surface is parallel to the grown layer in the $STO(001)_p//EuS(001)_p$ orientation. From this measurement we determine the $(001)_p$ lattice constant to be 6.06 Å, which indicates a strain of $\simeq 2\%$ from the known bulk lattice constant of 5.94 Å. Laue oscillations also occur near the layer's Bragg peak, which again indicates sharp surface/interface coherency. From these Laue oscillations, we can calculate the thickness (≈5 nm) of the grown layer, which matches quite well to the thicknesses monitored by the quartz crystal sensor during the growth.

We present representative magnetometry images (Fig. 2(a)-(c)) of the spatial modulation of ferromagnetism (Fig. 2(d)) on the micron scale when the heterostructure was trained (cooled through the Curie transition) with a 13 Gauss in-plane field. These scanning SQUID images were taken in the same cooldown at different locations on the sample. Note that the amplitude of the training field does not affect the features[45]. We defined the growth direction to be $[001]_p$. Unless indicated otherwise, the field training direction was pointed along the STO $[\bar{1}00]_p$ axis with respect to the original STO cubic crystal axes. The modulated ferromagnetic landscape appears as magnetic striations oriented along the $[110]_p$ direction (Fig. 2(a)), the $[010]_p$ direction (Fig. 2(b)), and along the $[100]_p$ direction (Fig. 2(c)). The

crystal directions were determined by knowledge of the growth direction and calibrated by scanning the edge of the sample pointing along the $[010]_p$ direction (Fig. 2(e)). The STO twin planes that intersect with the surface are along the $[100]_p$, $[110]_p$, $[1\bar{1}0]_p$, and $[010]_p$ directions. The fact that the observed magnetic features align exactly with these twin planes strongly suggests that the EuS magnetism is related to the STO tetragonal domain structure.

These images cannot describe the orientation of the spins contributing to the observed magnetic features because both in-plane and out-of-plane spins contribute to the z-component of the magnetic field. However any spatial variation in the density or the orientation of the spins would be detected and quantified by a scalar magnetic flux. Furthermore, the point-spread function of the SQUID pickup loop dictates the spatial resolution, any magnetic feature less than $\approx$ 3 μm is considered resolution-limited.

We quantitatively compared the measured magnetic flux at the edge of the sample with the expected magnetic flux for a given EuS magnetization density. The mean magnetic flux magnitude of a line cut through the edge of the sample was $\approx$80 mΦ_0, where $\Phi_0 = \frac{h}{2e}$ is the superconducting flux quantum. To compute the expected magnetic flux, we first compute the magnetization density. Taking the parameters of the EuS to be 28 μ_B/unit cell with a lattice constant of 0.59 nm[1] and a film thickness of 5 nm, we calculate an expected flux signal of approximately 200 mΦ_0[45], which is substantially larger than our measured signal at the edge. We attribute this difference to domain structure on smaller length scales than our spatial resolution, which reduces the total signal.

To determine the relative size of the observed magnetic modulation, we compared the peak-to-peak flux signal of the features to the flux signal at the edge of the sample. Taking a line cut of Fig. 2(c) (shown in Fig. 2(d)), we measured the mean peak-to-peak magnetic flux of the modulation for 5 peaks to be $\approx$55 mΦ_0 through the SQUID pickup loop. This magnetic flux is $\approx$ 65% of the flux signal at the edge, indicating that the observed spatial ferromagnetic variations are substantial.

The training field polarizes some of the spins along a specific direction, and to characterize how the spin polarization direction affects the formation of these magnetic features, we examined the dependence of the magnetic configuration on the in-plane training field direction (Fig. 3). Before acquiring each image, we thermal cycled the sample to 30 K, well above the expected Curie temperature of 16 K, and retrained the sample in a 13 Gauss field with different in-plane orientations. The magnetic features parallel to the $[100]_p$ and $[010]_p$ directions were independent of training-field direction, but the large magnetic features parallel to the $[110]_p$ direction disappeared for certain angles. This observation shows that the spin polarization orientation plays a role in the formation or visibility of these features.

To order to determine the Curie temperature T_C, we applied a 500 μA ac current (f = 514 Hz) to the field coil and performed a series of touchdowns to quantify the change in susceptibility with temperature. We performed touchdowns on the red cross (Fig. 4(a) and Fig. 4(b)), and we observed the susceptibility diverge as the temperature approached 15.5 K, indicating the ferromagnetic to paramagnetic transition (Fig. 4(c)). When we plotted the measured susceptibility when the SQUID was closest to the sample against temperature (Fig. 4(d)), we detected a divergence around 15.5 K associated with a ferromagnetic-to-paramagnetic transition. The error bars in Fig. 4(d) were determined by fitting bootstrapped touchdown data shown in Fig. 4(c) using the form for the susceptibility of a thin isotropic and monodomain paramagnet[4945]. The touchdown fits without bootstrapping shown in Fig. 4(c) clearly deviated from the measured data, perhaps because of uncertainty in the height calibration or unaccounted piezoelectric drift. The susceptibility for T > T_C measures the paramagnetic response of the sample, which we fit to the Curie Weiss law $\chi(T) = \frac{C}{T-T_C}$ (Fig. 4(d)), where T_C is the Curie temperature and C is a proportionality constant,

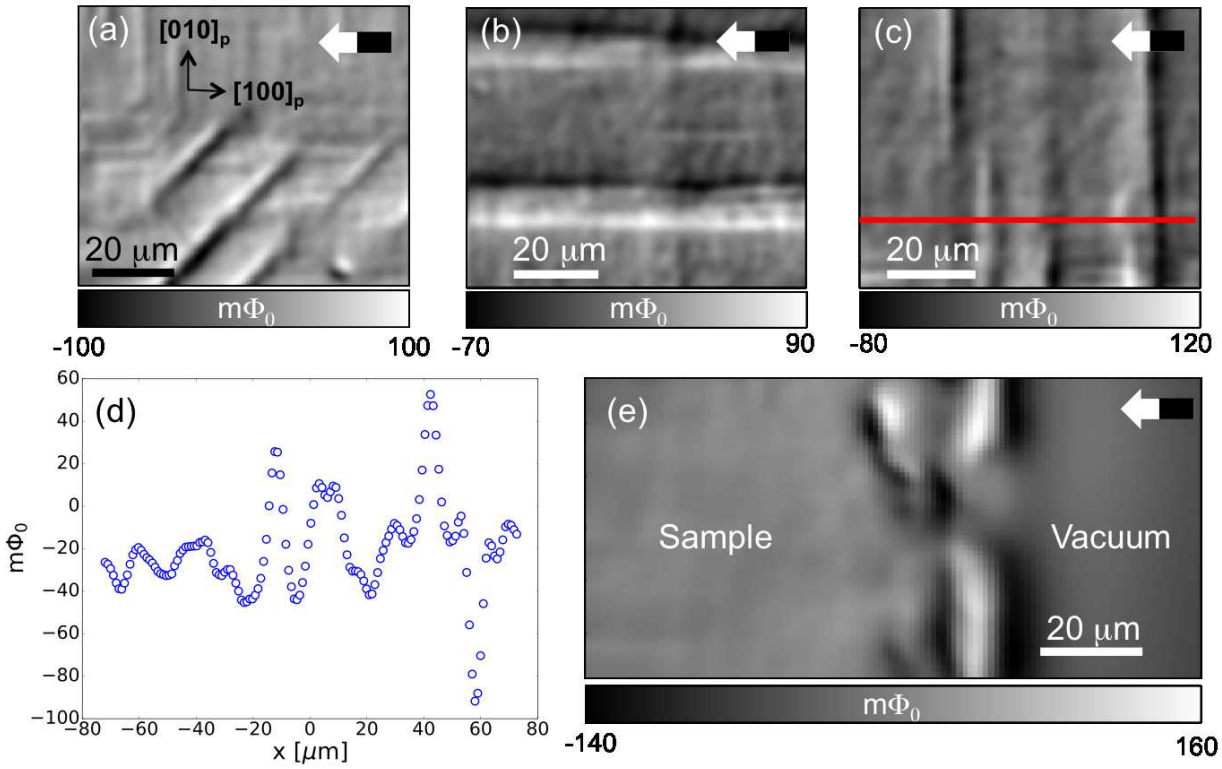

FIG. 2: Representative magnetometry images of EuS grown on STO showing modulated magnetic features that point primarily along the $[110]_p$ (a), $[010]_p$ (b), $[100]_p$ (c) STO crystallographic axes. The black and white arrows show the direction of the training field. A line cut of image (c), shown as the red line, is plotted in (d). The edge of the sample is shown in (e), allowing us to determine the STO pseudocubic axes that are labeled in (a).

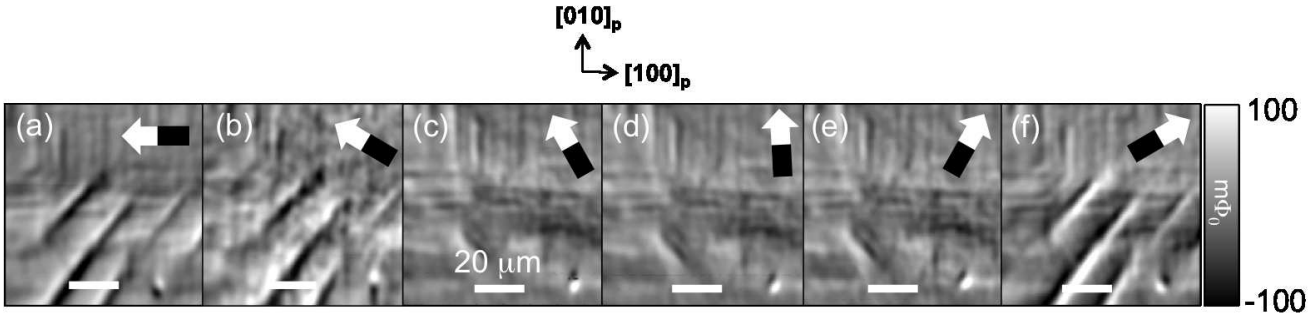

FIG. 3: Magnetometry dependence on in-plane field training angle. Before acquiring each image, we thermal cycled the sample to 30 K, well above the Curie temperature of EuS, and cooled with a 13 Gauss field in the direction specified by the arrow. With respect to the $[100]_p$ direction, the angle of the training field is (a) 180°, (b) 150°, (c) 120°, (d) 90°, (e) 60° and (f) 30°.

with T_C and C as the only free parameters. The Curie-Weiss law did not perfectly capture the data (Fig. 4(d)), perhaps due to height uncertainty and possible fluctuations close to T_C[2,12,13], but it does find the divergence-like peak in the paramagnetism. However, this fit yielded a fitted T_C = 15.4 K, which is similar to previously reported values for EuS[1]. As a check on our fitted T_C, we imaged the ferromagnetism with temperature (Fig. 4(e)-(k)) and found that the signal became indistinguishable from noise around 15.5 K, consistent with no ferromagnetic order.

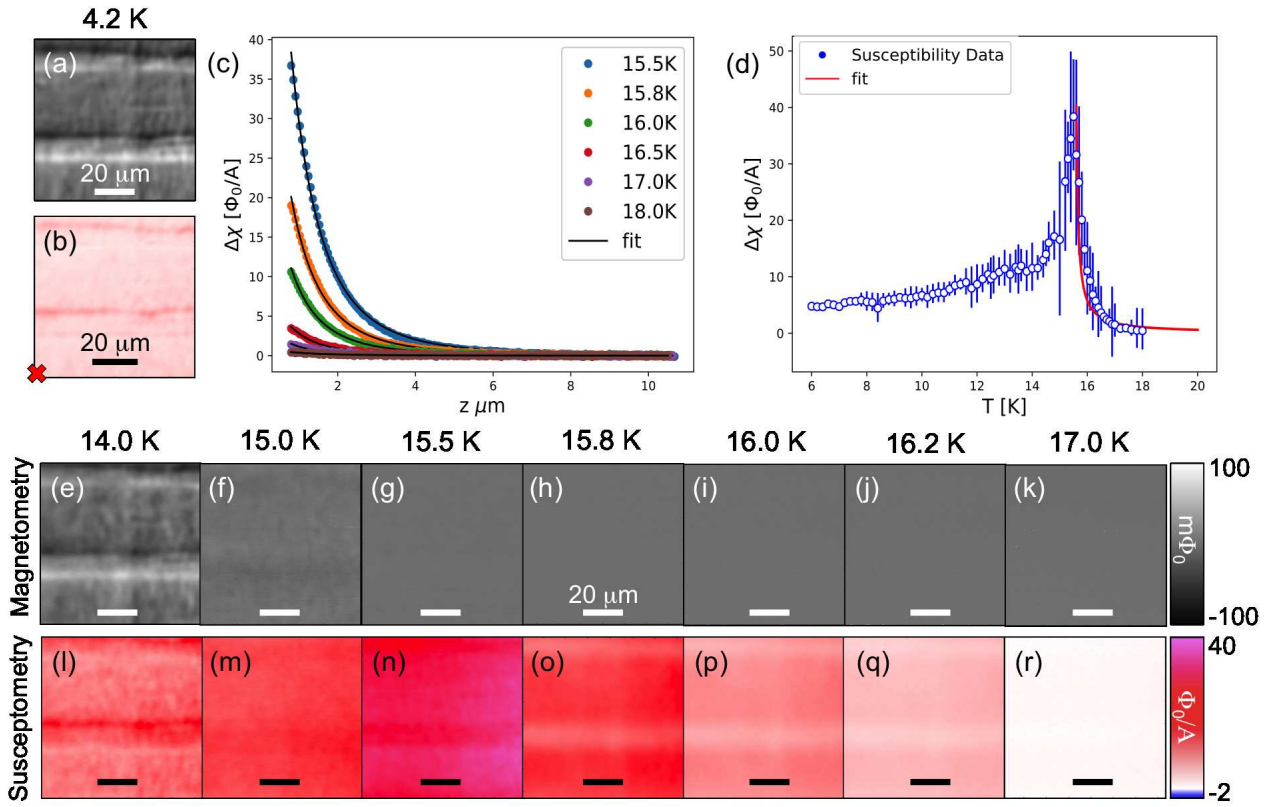

FIG. 4: Temperature dependence of the ferromagnetism and the susceptibility to determine the Curie temperature T_C. (a) Magnetometry image reproduced from Fig. 2(b), plotted with the corresponding (b) susceptibility image at 4.2 K. We performed susceptibility touchdowns as a function of temperature at the location in (b) marked with a red cross. (c) Representative touchdowns showing how the susceptibility changes with temperature close to and away from T_C. The height z is defined as the separation between the SQUID substrate and the sample surface. (d) Plot of the fitted susceptibility at z = 0 with temperature, including error bars as determined by bootstrapping. The susceptibility diverges, indicative of a paramagnetic-to-ferromagnetic phase transition. The paramagnetism above the Curie temperature is fit to a Curie-Weiss law with T_C = 15.4 K. (e) - (k) Magnetometry and (l) - (r) susceptibility images as a function of temperature. The paramagnetism above the fitted Curie temperature is spatially inhomogeneous, similar to the large ferromagnetic features below the Curie temperature at 4.2 K.

Images of the paramagnetism (Fig. 4(l)-(r)) above the Curie temperature showed similar spatially varying features as the ferromagnetism, suggesting that the paramagnetism is modified by a similar mechanism as the ferromagnetism.

To demonstrate that the observed magnetic behavior is due to the STO tetragonal structure, we studied how the ferromagnetic configuration changed with thermal history (Fig. 5(a)). Without any field training, the magnetometry image shows resolution-limited magnetic domains similar to SQUID measurements on conventional ferromagnets[50] (Fig. 5(b)), and we observe the magnetic striations when training in a small field (Fig. 5(c)). When thermal cycling above the Curie temperature to 30 K (Fig. 5(d)), the magnetic configuration does not have any distinct changes suggesting that the magnetic configuration is predetermined even before the EuS becomes ferromagnetic. However, when thermal cycling above 105 K, the magnetic configuration was substantially modified (compare Fig. 5(d) to Fig. 5(e) and Fig. 5(f) to Fig. 5(g)). Similar to the magnetic features in Fig. 2, all the features observed from thermal cycling point only along directions that intersect with twin planes, namely $[100]_p$ and $[010]_p$. Because the magnetic

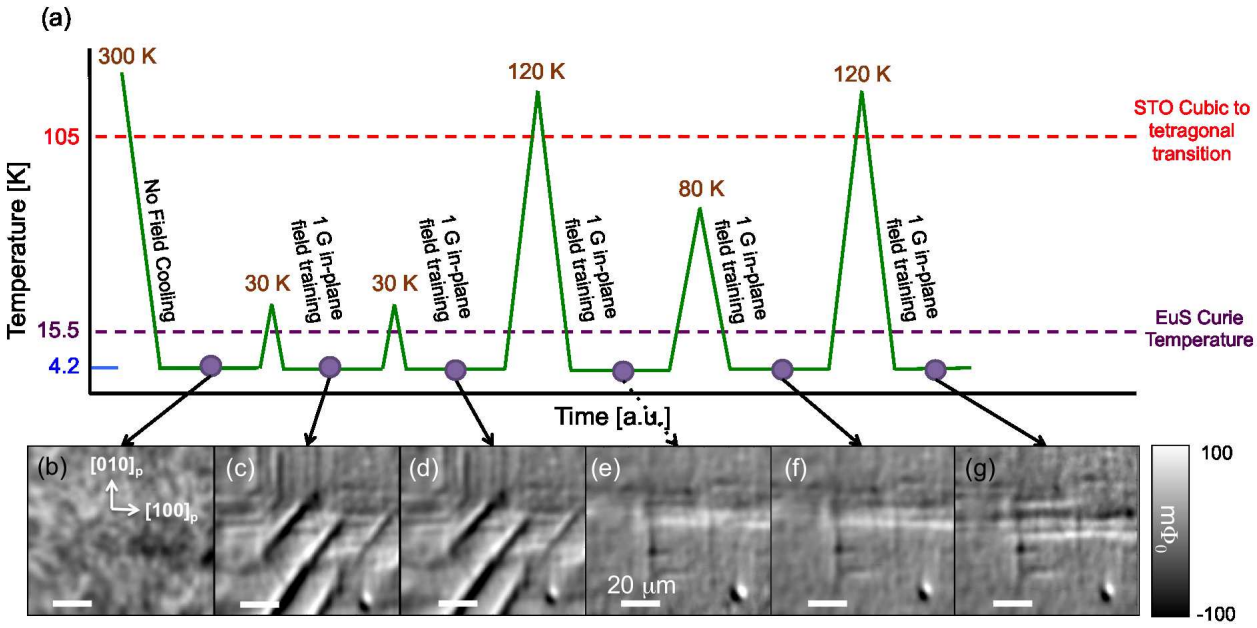

FIG. 5: Ferromagnetic spatial variations upon thermal cycling reveal a relationship between the magnetic structure and the STO structural phase transition. (a) Thermal history of one region; all images were taken at 4.2 K. (b) The sample was cooled from room temperature without field training, showing resolution-limited domains. (c) The sample was warmed above the Curie temperature of the EuS (30 K) and field trained with 1 Gauss, revealing a stripe-like magnetic configuration. The sample was then thermal cycled to (d) 30 K, (e) 120 K, (f) 80 K, and (g) 120 K, each cooled with a 1 Gauss field. From (d) to (e) and from (f) to (g), there are changes in the magnetic configuration corresponding to thermal cycling above the STO cubic-to-tetragonal phase transition, but the magnetic configuration does not change otherwise suggesting that the observed magnetic configuration is related to the STO structural phase transition.

features only changed when thermal cycling above the STO cubic-to-tetragonal transition, and because the features only pointed along twin plane directions, we conclude that the configuration of the EuS magnetism is coupled to the configuration of the STO twin structure. With this information, we conclude that the reason why the magnetic structures in 5(d) and 5(e) have so much contrast is because the STO forms tetragonal domains, and thermal cycling above the transition temperature will cause the domains to reshuffle. Because the real-space magnetic features are correlated with the underlying transition, the magnetic images should reshuffle as well. Because there is no external stain in the system, thermal cycling should not have any directional dependence.

We now discuss possible origins for the observed features. One possible explanation is that the modulated magnetism is due to topography on the surface of STO from the twin planes. Scanning single electron transistor studies have shown that the STO structural transition causes the twin boundaries between tetragonal domains to have a topographical kink with a change in slope of $\tan\alpha = \frac{1}{1000}$[43]. For larger boundaries between tetragonal domains, such as 15 - 20 μm, that kink can lead to topological variations as great as 5 nm[43]. Because the EuS is epitaxially grown on STO, the EuS could also experience this topography. The SQUID would measure a spatially dependent magnetic flux due to the height variation. We simulate the spatial magnetic flux from this topographical variation and find that this effect produces a spatially dependent magnetization that is two orders of magnitude smaller than the measured magnetic spatial variations[45]. We conclude that surface topography does not fully explain our results.

$\epsilon_{[100]_p}$	$K_{me,max}(x,y)$ [10^4 erg/cc]	$K_{me,max}/K_{mc}$
10^-5	$\simeq 0.018$	0.0075
10^-4	$\simeq 0.18$	0.075
10^-3	$\simeq 1.8$	0.75
10^-2	$\simeq 18$	7.5

TABLE I: For different strains ϵ we can compare the magnetoelatic energy $K_{me,max}(x,y)$ that can vary in space with the magnetocrystalline energy K_{mc}.

The coupling between the EuS magnetism and the STO tetragonal structure may be magnetoelastic in origin. EuS may experience a spatially dependent strain due to STO twin formation that may alter the magnetic anisotropy along the twin boundaries giving rise to the features observed in this work. Magnetic anisotropy is determined by magnetocrystalline energy and magnetoelastic energy, and we can compare these two energy scales to determine which has a stronger influence on the anisotropy. The magnetocrystalline energy for a cubic system is expressed as $E_{mc} = K_{mc}(\alpha_1^2\alpha_2^2 + \alpha_2^2\alpha_3^2 + \alpha_3^2\alpha_1^2)$ where $K_{mc} = 2.4 \times 10^4$ erg/cc and α_i are the directional cosines of the magnetization[51]. The magnetoelastic energy is expressed as $E_{me} = -K_{me}(x,y)\alpha_k\alpha_l$ where $K_{me} = \frac{3}{2}\lambda_{ijkl}\sigma_{ij}(x,y)$ and λ_{ijkl} is the magnetostriction coefficients, $\sigma_{ij}(x,y)$ is the stress from the STO twins in the x - y plane. Along the $[100]_p$ direction, the highest value $K_{me}(x,y)$ is when the strain is along the $[100]_p$ direction, which is expressed as $K_{me,max}(x,y) = \frac{3}{2}\lambda_{[100]_p}\sigma_{[100]_p}(x,y) = \frac{3}{2}\lambda_{[100]_p}c_{11}\epsilon_{[100]_p}(x,y)$ where c_{11} is the elastic modulus along the $[100]_p$ direction and $\epsilon(x,y)$ is the strain. Using values from the literature[52,53], $\lambda_{[100]_p} \simeq 10^{-5}$ and $c_{11} \simeq 120$ GPa, so $K_{me,max}(x,y) = 1.8 \times 10^7\epsilon(x,y)$ erg/cc. Note that $\lambda_{[100]_p}$ was experimentally determined for EuO, a related Eu chalcogenide.

To complete this calculation, we need to know $\epsilon(x,y)$. It is worth noting that X-ray diffraction measurements in Fig. 1(e) show that the out-of-plane lattice constant for 5 nm of EuS grown on STO has a strain of $\epsilon = 2 \times 10^{-2}$ at room temperature. However, this measured strain neglects how strain may vary spatially from twin formation, and calculating or experimentally determining the amount of strain for a thin film spatially is difficult. Instead, we remain agnostic as to how much strain is actually being applied, so we compare the magnetoelastic energy with the magnetocrystalline energy for a variety of strains, as shown in Table I. For small strains, the magnetocrystalline energy dominates, so the magnetoelastic energy will have a negligible affect on the anisotropy. However, for large strains that may occur from twin boundaries, the magnetoelastic energy will strongly influence the anisotropy, which may give rise to the spatially varying magnetic structure observed in this work.

Strain from twin formation in STO has been observed to alter the magnetic properties of $La_{2/3}Ca_{1/3}MnO_3$ (LCMO) and $La_{0.7}Ca_{0.3}MnO_3$ (LSMO) grown on STO, perhaps also arising from a magnetoelastic origin. Bulk magnetic measurements on LCMO grown on STO[54] and LSMO grown on STO[55] show changes in magnetization when cooled below the 105 K transition temperature, and micron-scale magnetic features similar to the ones reported here in Fig. 2 were observed via magneto-optic measurements[56]. The conclusion of that work is that strain from the STO twin structure causes a small out-of-plane rotation of the magnetic moments, which produces the observed spatial features in magnetism. However, this explanation is not necessarily applicable to this work because the origin of the magnetism in LCMO and EuS are different (respectively, double exchange[57] vs. indirect exchange[58]), and we have no evidence that the EuS magnetic moments have an out-of-plane component.

Much more information is needed to confirm a magnetoelastic argument. First, one could perform X-ray diffraction measurements as a function of temperature through the cubic to tetragonal phase transition to see how the EuS lattice constant changes, although these changes will be over a large length-scale so it would still be hard to map those measurements to the micron-scale SQUID results. Second, one could apply controlled uniaxial strain to the EuS/STO heterostructure and measure how the magnetism changes with a scanning SQUID or magneto-optic technique. Finally, density functional theory calculations could shed light on how a compressed lattice constant affects magnetism in EuS.

In conclusion, here we have shown that the STO tetragonal structure modifies the magnetism of an epitaxially coupled thin film of EuS. Understanding how structural changes influence magnetism may shed light on the fundamental basis of exchange interactions and lead to the development of new and interesting systems. Thus, these changes and their impact on magnetism need to be considered when constructing devices that require homogeneous magnetic exchange.

This work was supported by FAME, one of six centers of STARnet, a Semiconductor Research Corporation program sponsored by MARCO and DARPA. The SQUID microscope and sensors used were developed with support from the NSF-sponsored Center for Probing the Nanoscale at Stanford, NSF-NSEC 0830228, and from NSF IMR-MIP 0957616. F.K. and J.S.M. acknowledge the support from NSF Grants No. DMR-1207469, ONR Grant No. N00014-13-1- 0301 and N00014-16-1-2657, and the STC Center for Integrated Quantum Materials under NSF Grant No. DMR-1231319. N.G. and F.K. was supported by the STC Center for Integrated Quantum Materials under NSF grant DMR-1231319 (material growth). The authors also thank Adrian Swartz, Zheng Cui, Hilary Noad, and Eric Spanton for useful discussions as well as Sean Hart and Yuri Suzuki for assistance with the manuscript.

[1] A. Mauger and C. Godart, Physics Reports pp. 51–176 (1986).

[2] H. Idzuchi, Y. Fukuma, H. S. Park, T. Matsuda, T. Tanigaki, S. Aizawa, M. Shirai, D. Shindo, and Y. Otani, Applied Physics Express **7**, 113002 (2014).

[3] J. Kötzler and M. Muschke, Physical Review B **34**, 3543 (1986).

[4] T. Nagahama, T. Santos, and J. Moodera, Physical review letters **99**, 016602 (2007).

[5] P. LeClair, J. Ha, H. Swagten, J. Kohlhepp, C. Van de Vin, and W. De Jonge, Applied physics letters **80**, 625 (2002).

[6] G.-X. Miao, M. Müller, and J. S. Moodera, Physical review letters **102**, 076601 (2009).

[7] J. S. Moodera, T. S. Santos, and T. Nagahama, Journal of Physics: Condensed Matter **19**, 165202 (2007).

[8] X. Hao, J. Moodera, and R. Meservey, Physical Review B **42**, 8235 (1990).

[9] J. Moodera, X. Hao, G. Gibson, and R. Meservey, Physical review letters **61**, 637 (1988).

[10] H. Bohn, A. Kollmar, and W. Zinn, Physical Review B **30**, 6504 (1984).

[11] L. Passell, O. Dietrich, and J. Als-Nielsen, Physical Review B **14**, 4897 (1976).

[12] J. Als-Nielsen, O. Dietrich, W. Kunnmann, and L. Passell, Physical Review Letters **27**, 741 (1971).

[13] J. Als-Nielsen, O. Dietrich, and L. Passell, Physical Review B **14**, 4908 (1976).

[14] O. Dietrich, J. Als-Nielsen, and L. Passell, Physical Review B **14**, 4923 (1976).

[15] P. Wei, F. Katmis, B. A. Assaf, H. Steinberg, P. Jarillo-Herrero, D. Heiman, and J. S. Moodera, Physical review letters **110**, 186807 (2013).

[16] C. Lee, F. Katmis, P. Jarillo-Herrero, J. S. Moodera, and N. Gedik, Nature Communications **7** (2016).

[17] H. Zhang, C. X. Liu, X. L. Qi, X. Dai, Z. Fang, and S.-C. Zhang, Nature physics **5**, 438 (2009).

[18] Y. Zhang, K. He, C.-Z. Chang, C.-L. Song, L.-L. Wang, X. Chen, J.-F. Jia, Z. Fang, X. Dai, W.-Y. Shan, et al., Nature Physics **6**, 584 (2010).

[19] M. Bianchi, D. Guan, S. Bao, J. Mi, B. B. Iversen, P. D. King, and P. Hofmann, arXiv preprint arXiv:1009.2879 (2010).

[20] D. Kim, S. Cho, N. P. Butch, P. Syers, K. Kirshenbaum, S. Adam, J. Paglione, and M. S. Fuhrer, Nature Physics **8**, 459 (2012).

[21] W. Zhang, R. Yu, H.-J. Zhang, X. Dai, and Z. Fang, New Journal of Physics **12**, 065013 (2010).

[22] F. Katmis, V. Lauter, F. S. Nogueira, B. A. Assaf, M. E. Jamer, P. Wei, B. Satpati, J. W. Freeland, I. Eremin, D. Heiman, et al., Nature **533**, 513 (2016).

[23] M. Z. Hasan and C. L. Kane, Reviews of Modern Physics **82**, 3045 (2010).

[24] J. D. Sau, R. M. Lutchyn, S. Tewari, and S. D. Sarma, Physical review letters **104**, 040502 (2010).

[25] X.-L. Qi, T. L. Hughes, and S.-C. Zhang, Physical Review B **78**, 195424 (2008).

[26] A. M. Essin, J. E. Moore, and D. Vanderbilt, Physical review letters **102**, 146805 (2009).

[27] X.-L. Qi, R. Li, J. Zang, and S.-C. Zhang, Science **323**, 1184 (2009).

[28] R. B. Laughlin, Physical Review Letters **50**, 1395 (1983).

[29] C.-Z. Chang, J. Zhang, X. Feng, J. Shen, Z. Zhang, M. Guo, K. Li, Y. Ou, P. Wei, L.-L. Wang, et al., Science **340**, 167 (2013).

[30] W. Qing-Yan, L. Zhi, Z. Wen-Hao, Z. Zuo-Cheng, Z. Jin-Song, L. Wei, D. Hao, O. Yun-Bo, D. Peng, C. Kai, et al., Chinese Physics Letters **29**, 037402 (2012).

[31] X. Wu, D. Dijkkamp, S. Ogale, A. Inam, E. Chase, P. Miceli, C. Chang, J. Tarascon, and T. Venkatesan, Applied physics letters **51**, 861 (1987).

[32] J.-F. Ge, Z.-L. Liu, C. Liu, C.-L. Gao, D. Qian, Q.-K. Xue, Y. Liu, and J.-F. Jia, Nature materials **14**, 285 (2015).

[33] H. Sun, W. Tian, X. Pan, J. H. Haeni, and D. G. Schlom, Applied physics letters **84**, 3298 (2004).

[34] J. Jiang, X. Pan, W. Tian, C. Theis, and D. Schlom, Applied Physics Letters **74**, 2851 (1999).

[35] A. Caviglia, M. Gabay, S. Gariglio, N. Reyren, C. Cancellieri, and J.-M. Triscone, Physical review letters **104**, 126803 (2010).

[36] S. Klimin, J. Tempere, D. van der Marel, and J. Devreese, Physical Review B **86**, 045113 (2012).

[37] C. Koonce, M. L. Cohen, J. Schooley, W. Hosler, and E. Pfeiffer, Physical Review **163**, 380 (1967).

[38] A. Ohtomo and H. Hwang, Nature **427**, 423 (2004).

[39] S. Thiel, G. Hammerl, A. Schmehl, C. Schneider, and J. Mannhart, Science **313**, 1942 (2006).

[40] N. Reyren, S. Thiel, A. Caviglia, L. F. Kourkoutis, G. Hammerl, C. Richter, C. Schneider, T. Kopp, A.-S. Rüetschi, D. Jaccard, et al., Science **317**, 1196 (2007).

[41] R. Cowley, Physical Review **134**, A981 (1964).

[42] B. Kalisky, E. M. Spanton, H. Noad, J. R. Kirtley, K. C. Nowack, C. Bell, H. K. Sato, M. Hosoda, Y. Xie, Y. Hikita, et al., Nature materials **12**, 1091 (2013).

[43] M. Honig, J. A. Sulpizio, J. Drori, A. Joshua, E. Zeldov, and S. Ilani, Nature materials **12**, 1112 (2013).

[44] H. Noad, E. M. Spanton, K. C. Nowack, H. Inoue, M. Kim, T. A. Merz, C. Bell, Y. Hikita, R. Xu, W. Liu, et al., Physical Review B **94**, 174516 (2016).

[45] See Supplemental Material at [URL will be inserted by publisher] for measurements on additional samples, training field dependence on the modulated magnetism, magnetic flux simulations exploring potential origins of the modulated ferromagnetism, and how paramagnetism is quantified.

[46] E. H. Brandt, Physical Review B **72**, 024529 (2005).

[47] J. R. Kirtley, L. Paulius, A. J. Rosenberg, J. C. Palmstrom, C. M. Holland, E. M. Spanton, D. Schiessl, C. L. Jermain, J. Gibbons, Y.-K.-K. Fung, et al., Review of Scientific Instruments **87**, 093702 (2016).

[48] M. E. Huber, N. C. Koshnick, H. Bluhm, L. J. Archuleta, T. Azua, P. G. Björnsson, B. W. Gardner, S. T. Halloran, E. A.

Lucero, and K. A. Moler, Review of Scientific Instruments **79**, 053704 (2008).

[49] J. Kirtley, B. Kalisky, J. Bert, C. Bell, M. Kim, Y. Hikita, H. Hwang, J. Ngai, Y. Segal, F. Walker, et al., Physical Review B **85**, 224518 (2012).

[50] T. Higgs, S. Bonetti, H. Ohldag, N. Banerjee, X. Wang, A. Rosenberg, Z. Cai, J. Zhao, K. Moler, and J. Robinson, Scientific Reports **6** (2016).

[51] M. Franzblau, G. E. Everett, and A. Lawson, Physical Review **164**, 716 (1967).

[52] B. Argyle and N. Miyata, Physical Review **171**, 555 (1968).

[53] Q. Liu and F. Peng, Chinese Journal of Chemical Physics **27**, 387 (2014).

[54] M. Ziese, I. Vrejoiu, A. Setzer, A. Lotnyk, and D. Hesse, New Journal of Physics **10**, 063024 (2008).

[55] E. Wahlström, F. Macià, J. E. Boschker, Å. Monsen, P. Nordblad, R. Mathieu, A. D. Kent, and T. Tybell, New J. Phys **19**, 063002 (2017).

[56] V. Vlasko-Vlasov, Y. Lin, D. Miller, U. Welp, G. Crabtree, and V. Nikitenko, Physical review letters **84**, 2239 (2000).

[57] K. Ghosh, C. Lobb, R. Greene, S. Karabashev, D. Shulyatev, A. Arsenov, and Y. Mukovskii, Physical review letters **81**, 4740 (1998).

[58] I. Goncharenko and I. Mirebeau, Physical review letters **80**, 1082 (1998).